

recent observation that activation of P2X receptors on neurites of identified nociceptors induces firing of action potentials<sup>20</sup>. In that study<sup>20</sup> it was suggested that P2X receptors localized at peripheral sensory nerve terminals provide a mechanism for sensing nociceptive stimulation. Thus it is possible that P2X receptors expressed on both the peripheral terminals and central presynaptic terminals are capable of modulating or generating nociceptive signalling. □

## Methods

**Cell cultures.** Monocultures of dorsal horn neurons were prepared as described<sup>21</sup>. For DRG–dorsal horn co-cultures, dorsal horn neurons were isolated from rat embryos aged 16 days (E16) *in utero*, exposed to 0.25% trypsin for 20 min and dissociated. Similarly, DRGs were isolated separately from E16 embryos, exposed to trypsin and dissociated. Dorsal horn and DRG neurons were plated on glass coverslips previously prepared with a monolayer of rat cortical astrocytes. At the time of plating, 2.5S NGF (10 ng ml<sup>-1</sup>) and 5-fluoro-2'-deoxyuridine (10 µM) were added, and 2.5S NGF was added once every week when cells were fed with fresh media. For dorsal horn plus DRG explant cultures, conditions were the same except that the ganglia were isolated and plated directly on the centre of the glass coverslips. Micro-island cultures<sup>22</sup> were prepared as follows. Coverslips were precoated with PDL then dipped in 0.5% agarose (type I, low EEP; Sigma) and allowed to dry for 1 h. Once dry, the dishes were sprayed with rat-tail collagen (2 mg ml<sup>-1</sup> in a 0.2% acetic acid solution) using an atomizer. The dishes were sterilized by ultraviolet irradiation for 2 h, then plated with astrocytes. After 3–7 days, neurons were plated on top of the astrocytes. The plating density was usually 10,000–30,000 dorsal horn neurons per dish, and 30,000–50,000 DRG neurons per dish. Cultures at 2–4 weeks were used for experiments. In some experiments, DRG cell bodies were removed for co-culture dishes before experiments, and dorsal horn neurons and remaining DRG fibres stayed healthy for at least 2 h.

**Electrophysiology recordings.** Standard bathing solution contained (in mM): 145 NaCl, 5 KCl, 2 CaCl<sub>2</sub>, 2 MgCl<sub>2</sub>, 10 HEPES, 5.5 D-glucose, and 5 × 10<sup>-4</sup> TTX, pH 7.3 with NaOH, 325 mOsm with sucrose, flow rate of 1 ml min<sup>-1</sup>, and room temperature. Bicuculline (10 µM) and strychnine (5 µM) were also present. Dorsal horn neurons were voltage-clamped<sup>21</sup> at -70 mV in perforated whole-cell patch configuration (Axopatch 200) with electrodes containing internal solution (in mM): 75 Cs<sub>2</sub>SO<sub>4</sub>, 10 CsCl, 0.1 CaCl<sub>2</sub>, 10 HEPES and 400 µg ml<sup>-1</sup> amphotericin B, pH 7.3 with CsOH and 315–325 mOsm with sucrose. For experiments on ATP-evoked glutamate release, 200 µM ATP was puffed for 100 ms with puff pipettes of 1.5–2 µm diameter at 3.5–6.5 p.s.i. Recovery periods (4–8 min) were allowed between ATP applications except when otherwise specified. For experiments testing pharmacology of ATP-evoked currents, cells were rested in normal bathing solution for ~8 min to allow recovery from desensitization caused by previous trials. CNQX (100 µM), La<sup>3+</sup> (30 µM) and PPADS (50 µM) were preapplied to the bathing solution for 2–4 min. Effects of P2X receptor activation on spontaneous glutamate release from presynaptic terminals of DRG neurons were determined by measuring the effects of 100 µM ATP and 100 µM αβm-ATP on mEPSCs recorded from dorsal horn neurons. Cultures were perfused with standard bathing solution plus 10 mM lidocaine. mEPSCs were recorded from dorsal horn neurons voltage-clamped at -70 mV in perforated patch configuration<sup>21</sup>. After 5 min recording of control mEPSCs, 100 µM ATP or αβm-ATP was bath-applied for 5 min and mEPSCs were continuously recorded. Effects of PPADS were tested following wash of ATP for several minutes to allow mEPSCs to return to the basal control conditions. After 3–5 min of pre-applying 50 µM PPADS, ATP and 50 µM PPADS were then coapplied and mEPSCs recorded. In experiments measuring mEPSCs in low extracellular Ca<sup>2+</sup> concentrations, the bathing solution was the same as the standard bathing solution except that Ca<sup>2+</sup> was not added. In experiments with La<sup>3+</sup>, 30 µM La<sup>3+</sup> was present at all times in bathing solution and ATP was applied with 30 µM La<sup>3+</sup>. Thus, although basal mEPSC frequency was found to be affected by 30 µM La<sup>3+</sup>, ATP always increased mEPSC frequency above that in La<sup>3+</sup>. mEPSC sampling and data analysis were done as described<sup>21</sup>. Electrophysiological recordings from DRG neurons were made using conventional whole-cell voltage clamps at -70 mV with patch electrodes containing intracellular solution of (in mM): 130 Cs-gluconate, 10 CsCl, 11 EGTA, 1 CaCl<sub>2</sub>, 10 HEPES, 20 TEA, 2 ATP-Mg, 305 mOsm, pH 7.2. A paired Wilcoxon test was

used for statistical analysis of the mean mEPSC frequency and amplitude under different experimental conditions.

Received 24 March; accepted 17 July 1997.

1. Burnstock, G. in *P2 Purinoceptors: Localization, Function and Transduction Mechanisms* (eds Chadwick, D. J. & Goode, J. A.) 1–34 (Wiley, New York, 1996).
2. North, R. A. in *P2 Purinoceptors: Localization, Function and Transduction Mechanisms* (eds Chadwick, D. J. & Goode, J. A.) 91–109 (Wiley, New York, 1996).
3. Chen, C.-C. *et al.* A P2X purinoceptor expressed by a subset of sensory neurons. *Nature* **377**, 428–431 (1995).
4. Lewis, C. *et al.* Coexpression of P2X<sub>2</sub> and P2X<sub>3</sub> receptor subunits can account for ATP-gated currents in sensory neurons. *Nature* **377**, 432–435 (1995).
5. Vulchanova, L. *et al.* Differential distribution of two ATP-gated ion channels (P2X receptors) determined by immunocytochemistry. *Proc. Natl Acad. Sci. USA* **93**, 8063–8067 (1996).
6. Roy, M. L. & Narashi, T. Differential properties of tetrodotoxin-sensitive and tetrodotoxin-resistant sodium channels in rat dorsal root ganglion neurons. *J. Neurosci.* **12**, 2104–2111 (1992).
7. McLaren, G. J. *et al.* Investigation of the actions of PPADS, a novel P2X-purinoceptor antagonist, in the guinea-pig isolated vas deferens. *Br. J. Pharmacol.* **111**, 913–917 (1994).
8. Behnam, C. D. & Tsien, R. W. A novel receptor-operated Ca<sup>2+</sup>-permeable channel activated by ATP in smooth muscle. *Nature* **328**, 275–278 (1987).
9. Nakazawa, K., Fujimori, K., Takanaka, A. & Inoue, K. An ATP-mediated conductance in pheochromocytoma cells and its suppression by extracellular calcium. *J. Physiol. (Lond.)* **428**, 257–272 (1990).
10. Rogers, M. & Dani, J. Comparison of quantitative calcium flux through NMDA, ATP, and ACh receptor channels. *Biophys. J.* **68**, 501–506 (1995).
11. Bean, P. B. & Williams, C. A. & Ceelen, P. W. ATP-activated channels in rat and bullfrog sensory neurons: current-voltage relation and single-channel behavior. *J. Neurosci.* **10**, 11–19 (1990).
12. Reichling, D. B. & MacDermott, A. B. Lanthanum actions on excitatory amino acid-gated currents and voltage-gated calcium currents in rat dorsal horn neurons. *J. Physiol. (Lond.)* **441**, 199–218 (1991).
13. Bardoni, R., Goldstein, P., Lee, J., Gu, J. G. & MacDermott, A. B. ATP P2X receptors mediate fast synaptic transmission in the dorsal horn of spinal cord. *J. Neurosci.* **17**, 5297–5304 (1997).
14. Krishtal, O. A., Marchenko, S. M. & Pidoplichko, V. I. Receptor for ATP in the membrane of mammalian sensory neurons. *Neurosci. Lett.* **35**, 41–45 (1983).
15. McGehee, D. S., Heath, M. J. S., Gelber, S., Devay, P. & Role, L. W. Nicotine enhancement of fast excitatory synaptic transmission in CNS by presynaptic receptors. *Science* **269**, 1692–1696 (1995).
16. Li, J. & Perl, E. R. ATP modulation of synaptic transmission in the spinal substantia gelatinosa. *J. Neurosci.* **15**, 3357–3365 (1995).
17. White, T. D., Downie, J. W. & Leslie, R. A. Characteristics of K<sup>+</sup>- and veratridine-induced release of ATP from synaptosomes prepared from dorsal and ventral spinal cord. *Brain Res.* **334**, 372–374 (1985).
18. Gray, R., Rajan, A. S., Radcliffe, K. A., Yakehiro, M. & Dani, J. A. Hippocampal synaptic transmission enhanced by low concentrations of nicotine. *Nature* **383**, 713–716 (1996).
19. Liu, H., Mantyh, P. W. & Basbaum, A. I. NMDA-receptor regulation of substance P release from primary afferent nociceptors. *Nature* **386**, 721–724 (1997).
20. Cook, S. P., Vulchanova, L., Hargreaves, K. M., Elde, R. & McCleskey, E. W. Distinct ATP receptors on pain-sensing and stretch-sensing neurons. *Nature* **387**, 505–508 (1997).
21. Gu, J. G., Albuquerque, C., Lee, C. J. & MacDermott, A. B. Synaptic strengthening through activation of Ca<sup>2+</sup>-permeable AMPA receptors. *Nature* **381**, 793–796 (1996).
22. Segal, M. M. & Furshpan, E. J. Epileptiform activity in microcultures containing small numbers of hippocampal neurons. *J. Neurophysiol.* **64**, 1390–1399 (1990).

**Acknowledgements.** We thank S. Siegelbaum, L. W. Role and J. Koester for comments on an early version of the manuscript; C. Albuquerque and A. Shang for help in developing the micro-island co-cultures; and S. Rappaport for advice. This work was supported by the MRC Fellowship of Canada (J.G.G.) and the NIH and Whitehall Foundation (A.B.M.).

Correspondence and requests for materials should be addressed to J.G.G. (e-mail: jg147@columbia.edu).

## Molecular basis of agonism and antagonism in the oestrogen receptor

Andrzej M. Brzozowski\*, Ashley C. W. Pike\*, Zbigniew Dauter\*, Roderick E. Hubbard\*, Tomas Bonn†, Owe Engström†, Lars Öhman†, Geoffrey L. Greene‡, Jan-Åke Gustafsson§ & Mats Carlquist†

\* Protein Structure Group, Chemistry Department, University of York, York YO1 5DD, UK

† Karo Bio AB, NOVUM, S-141 57 Huddinge, Sweden

‡ The Ben May Institute for Cancer Research, The University of Chicago, 5841 S. Maryland Ave, Chicago, Illinois 60637, USA

§ Karolinska Institute, S-141 86 Huddinge, Sweden

|| These authors contributed equally to this work.

Oestrogens are involved in the growth, development and homeostasis of a number of tissues<sup>1</sup>. The physiological effects of these steroids are mediated by a ligand-inducible nuclear transcription factor, the oestrogen receptor (ER)<sup>2</sup>. Hormone binding to the ligand-binding domain (LBD) of the ER initiates a series of molecular events culminating in the activation or repression of

target genes. Transcriptional regulation arises from the direct interaction of the ER with components of the cellular transcription machinery<sup>3,4</sup>. Here we report the crystal structures of the LBD of ER in complex with the endogenous oestrogen, 17 $\beta$ -oestradiol, and the selective antagonist raloxifene<sup>5</sup>, at resolutions of 3.1 and 2.6 Å, respectively. The structures provide a molecular basis for the distinctive pharmacophore of the ER and its catholic binding properties. Agonist and antagonist bind at the same site within the core of the LBD but demonstrate different binding modes. In addition, each class of ligand induces a distinct conformation in the transactivation domain of the LBD, providing structural evidence of the mechanism of antagonism.

The structure of the complex between ER's LBD and the antagonist raloxifene (RAL) was determined by conventional multiple isomorphous replacement in combination with multicrystal averaging, and was subsequently used as a phasing model in molecular replacement to solve the structure of the complex of the LBD

with 17 $\beta$ -oestradiol (E<sub>2</sub>) (see Methods and Table 1). The overall architecture of the ER LBD (helices H3–H12) is similar to that seen in the crystal structures of other nuclear receptor LBDs<sup>6–8</sup>, and emphasizes the universal nature of this fold within this receptor superfamily<sup>9</sup>. The LBD is folded into a three-layered antiparallel  $\alpha$ -helical sandwich comprising a central core layer of three helices (H5/6, H9 and H10) sandwiched between two additional layers of helices (H1–4 and H7, H8, H11). This helical arrangement creates a 'wedge-shaped' molecular scaffold that maintains a sizeable ligand-binding cavity at the narrower end of the domain. The remaining secondary structural elements, a small two-stranded antiparallel  $\beta$ -sheet (S1 and S2) and H12, are located at this ligand-binding portion of the molecule, and flank the main three-layered motif (Fig. 1a).

The ER LBDs are arranged as non-crystallographic dimers within both the E<sub>2</sub> and RAL complex crystals in a manner consistent with both the oligomeric state of liganded ER in solution<sup>10</sup> and previous

**Table 1** Data collection, phase determination and refinement statistics

	ER RAL	ER E <sub>2</sub>	ER RAL derivatives		
			PCMBs-1 (4 mM, 5 day)	PCMBs-2 (4 mM, 14 day)	KAu(CN) <sub>2</sub> (4 mM, 2 day)
Resolution (Å)	25–2.6	20–3.1	20–3	20–3	20–3.6
Unique reflections	15,433	33,981	10,335	9,316	5,835
Completeness (%)	95.7	99.1	97.6	89.0	94.2
Multiplicity	4.5	2.5	4	3.1	2.5
R <sub>sym</sub> (I)†	8.0	10.0	8.1	9.2	7.0
R <sub>iso</sub> †			16.9	20.7	13.7
Phasing power (centric/acentric)‡			1.22/1.88	1.23/2.02	0.71/0.94
R <sub>Cullis</sub> (centric/acentric)§			0.75/0.68	0.76/0.66	0.90/0.85
Refinement					
Reflections used (R <sub>free</sub> set)	13,868 (1,565)	30,583 (3,398)			
R <sub>cryst</sub> (R <sub>free</sub> )	21.9 (29.9)	21.8 (25.1)			
Protein (solvent) atoms	3,633 (100)	11,382 (114)			
% A,B,L (a,b,l,p)¶	94.2 (5.8)	94.2 (5.8)			
R.m.s.d. bond lengths/angles (Å)#	0.016/0.035	0.011/0.039			
R.m.s.d. n.c.s. protein (Å)*	0.66	0.07			
R.m.s.d. n.c.s. B (Å <sup>2</sup> )**	7.9	1.15			

\*R<sub>sym</sub> (I) = 100 ×  $\sum_i \sum_j |I_i - I_j| / \sum_i I_i$ , where I is the observed intensity, I<sub>j</sub> is the average intensity of multiple observations of symmetry-related reflections.

†R<sub>iso</sub> =  $\sum_i |F_{PH}| - |F_P| / \sum_i |F_{PH}|$ , where |F<sub>P</sub>| is the protein structure factor amplitude and |F<sub>PH</sub>| is the heavy-atom derivative structure factor amplitude.

‡Phasing power for centric and acentric reflections = r.m.s. (|F<sub>H</sub>|/|E|), where F<sub>H</sub> is the heavy atom structure factor amplitude and E is the residual lack of closure error.

§R<sub>Cullis</sub> =  $\sum_i |E| / \sum_i |F_{PH}| - |F_P|$  for centric and acentric reflections. Figure of merit was 0.48 for acentric reflections and 0.67 for centric reflections (20–3 Å).

||R<sub>cryst</sub> = 100 ×  $\sum_i |F_{PH}| - |F_P| / \sum_i |F_{PH}|$ ; R<sub>free</sub> is the same as R<sub>cryst</sub> but was calculated using a separate validation set of reflections that was excluded from the refinement process.

¶Percentage of residues located in most favoured (additional) regions of the Ramachandran plot as determined by PROCHECK<sup>20</sup>.

#R.m.s. deviation in bond length and angle distances from Engh and Huber ideal values.

\*Root mean squared distance between all non-crystallographic symmetry (n.c.s.) related protein atom positions.

\*\*R.m.s. difference between all n.c.s.-related atomic temperature factors.

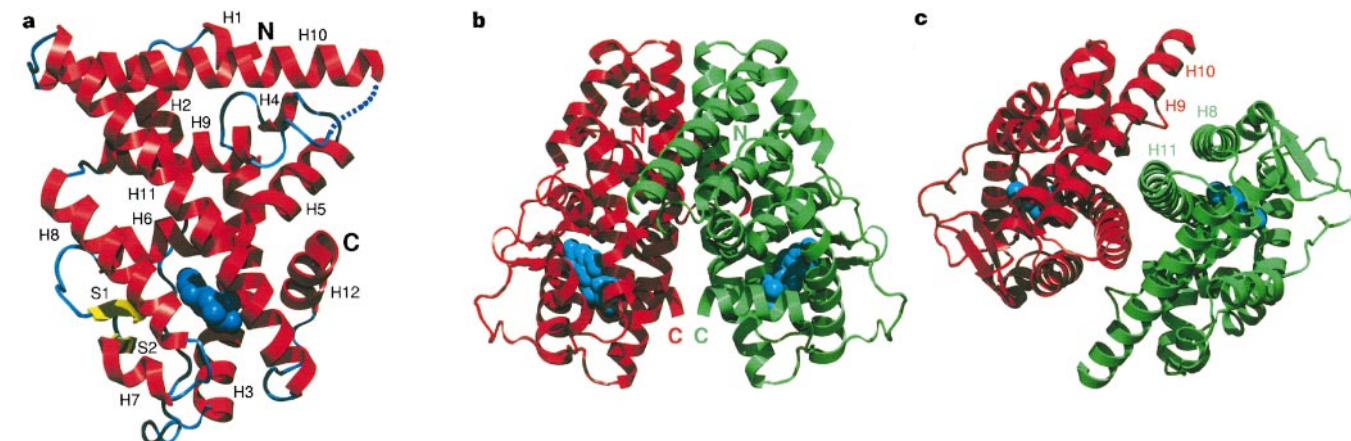


**Figure 1** Ribbon representations of the ER- $\alpha$  LBD. **a**, The ER- $\alpha$  LBD indicating the locations of the secondary structural elements.  $\alpha$  and  $3_{10}$  helices (H) are coloured red, extended regions (S) are yellow, and coil regions are blue. All secondary structural elements have been numbered in keeping with the nomenclature that has been established for other nuclear receptor LBDs. The monomer is displayed looking onto the dimerization face. The dotted line indicates the unmodelled

region between H9 and H10. **b**, ER- $\alpha$  LBD homodimer viewed perpendicular to the dimer axis. **c**, ER- $\alpha$  LBD homodimer viewed down the dimer axis. The component monomers are drawn in red and green. The N and C termini and the helices that are involved in the dimer interface are labelled. E<sub>2</sub> is coloured blue and depicted in space-filling form.

mutagenesis studies<sup>11</sup>. All crystal forms of the liganded ER LBD obtained so far contain identical non-crystallographic dimers (data not shown). The overall homodimeric arrangement is the same in both the E<sub>2</sub> and RAL complexes, and is reminiscent of the crystallographic apo-retinoid-X receptor homodimer<sup>8</sup>. The dimer axis roughly coincides with the longest dimension of the LBD with each molecule tilted approximately 10° away from the two-fold axis. This symmetric 'head-to-head' arrangement locates the chain termini of each monomer on opposite sides of the dimer with the carboxy termini projecting towards the two-fold axis (Fig. 1b). The H8/H11 face of the monomers line up to form an extensive dimerization interface that encompasses about 15% (1,703 Å<sup>2</sup>) of each monomer's surface area. Contacts between the two molecules are made primarily through the H11 helices, which intertwine to form a rigid backbone, but also involve H8 from one monomer and parts of H9 and H10 from the neighbouring monomer (Fig. 1c).

The E<sub>2</sub> binding cavity is completely partitioned from the external environment and occupies a relatively large portion of the ER LBD's hydrophobic core (Fig. 1a). It is located at one end of the molecule and is formed by parts of H3 (Met 342 to Leu 354), H6 (Trp 383 to Arg 394), H8 and the preceding loop (Val 418 to Leu 428), H11 (Met 517 to Met 528), H12 (Leu 539 to His 547) and the S1/S2 hairpin (Leu 402 to Leu 410). Hormone recognition is achieved through a combination of specific hydrogen bonds and the complementarity of the binding cavity to E<sub>2</sub>'s non-polar character (Fig. 2a,c). E<sub>2</sub> binds diagonally across the cavity between H11, H3 and H6 and adopts a low-energy conformation. The phenolic hydroxyl of the A-ring (O3; see Fig. 2c for atom numbering) nestles between H3 and H6 and makes direct hydrogen bonds to the carboxylate of Glu 353, the guanidinium group of Arg 394, and a water molecule. The 17-β hydroxyl (O17) of the D-ring makes a single hydrogen bond with His 524. The remainder of the molecule participates in a number of hydrophobic

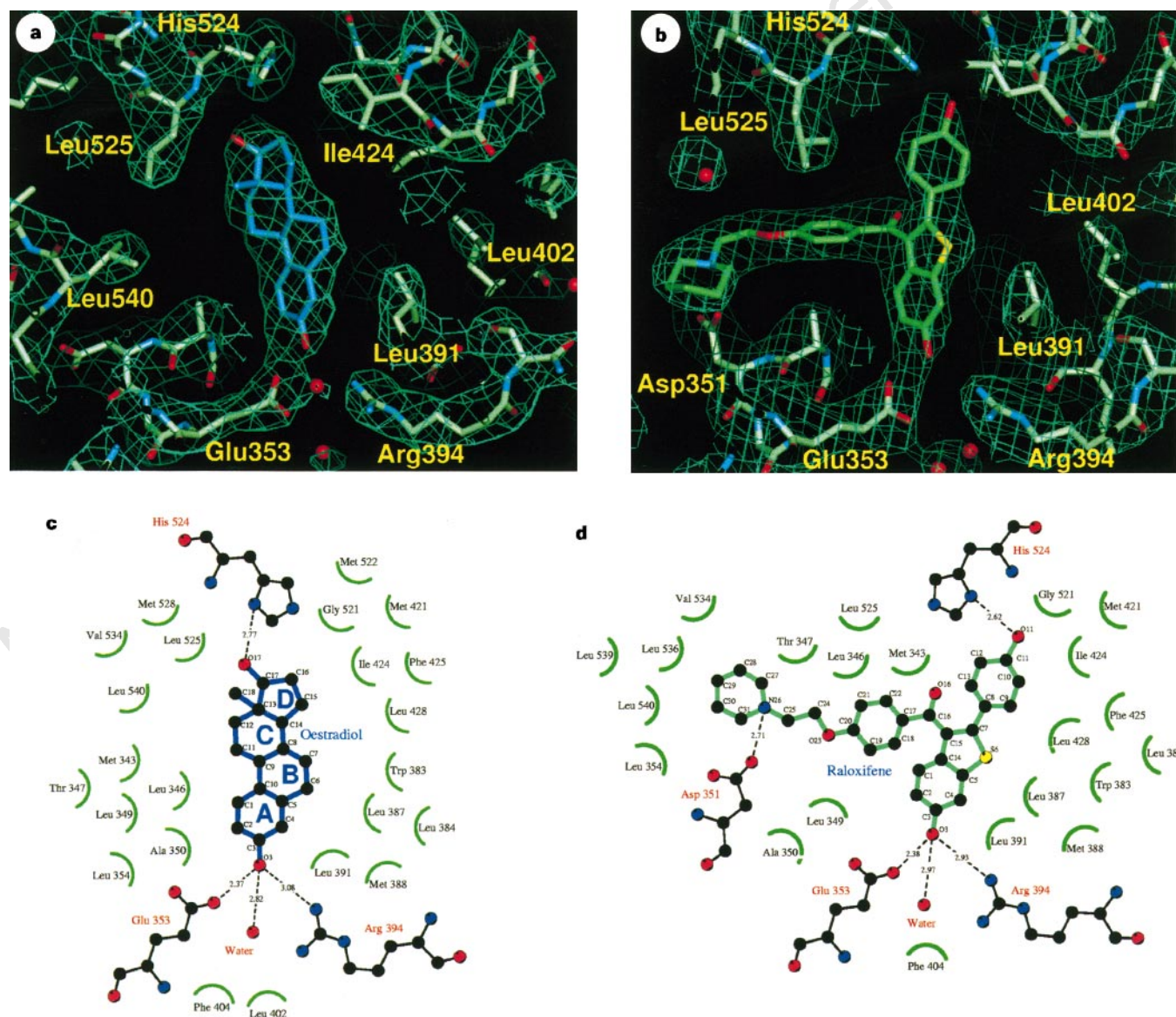


**Figure 2** Agonist and antagonist binding modes. **a**, The 3.1-Å resolution, six-fold averaged electron-density map (using model phases) for the ER LBD-E<sub>2</sub> complex. **b**, The experimental, 2.6-Å resolution electron-density map for the ER LBD-RAL complex after DMMULTI multicrystal averaging. In both cases, the map is contoured at 1σ and overlaid on the final refined models. **c**, **d**, Schematic representation of the interactions made by E<sub>2</sub> (**c**) and RAL (**d**) within the binding

cavity. Residues that interact with ligand and/or line the cavity are shown in their approximate positions. Those that make direct hydrogen bonds are depicted in ball-and-stick style with broken lines between the interacting atoms. The hydrogen-bond distances shown are averaged between the six (E<sub>2</sub>) or two (RAL) monomers. The atom names and ring nomenclature of E<sub>2</sub> are also given.



contacts that are concentrated over the A, A/B interface and D-rings. The A-ring, as well as the planar A/B-ring interface, is sandwiched between the side chains of Ala 350 and Leu 387 on its  $\beta$  face and Phe 404 on its  $\alpha$  face. At the other end of the binding cavity, the D-ring makes non-polar contacts with Ile 424, Gly 521 and Leu 525. Although the cavity itself appears to be devoid of ordered water molecules, an extensive solvent channel runs from the A-ring hydroxyl's water ligand to the exterior of the LBD between H3 and H5/6. The combination of the specific polar and non-polar interactions account for the ability of ER to selectively recognize and bind  $E_2$  with subnanomolar affinity over the large and varied range of endogenous steroids.

Extensive binding studies of  $E_2$  analogues have provided a detailed description of the pharmacophore of ER<sup>12</sup>. The ER is unique among the steroid receptors in its ability to embrace a wide variety of non-steroidal compounds. Although the 'pincer-like' arrangement around the A-ring imposes an absolute requirement on effective ligands to contain an aromatic ring, the remainder of the binding pocket can accept a number of different hydrophobic groups<sup>12,13</sup>. This overall promiscuity can be attributed to the size of the cavity, which has a probe accessible volume (450 Å<sup>3</sup>) nearly twice that of  $E_2$ 's molecular volume (245 Å<sup>3</sup>). The length and breadth of the  $E_2$  skeleton is well matched by the receptor, but there are large unoccupied cavities opposite the  $\alpha$  face of the B-ring and the  $\beta$  face of the C-ring (Fig. 2a). The positions of these preformed cavities are similar to those predicted from binding studies<sup>12</sup>.

This structure is the first example of an LBD from the steroid class of nuclear receptors, and provides an instructive model for members of this family. A similar overall hormone-binding mode is anticipated with the A-ring probably bound between H3 and H6 by an arginine (homologue of Arg 394) and a glutamine (homologue of Glu 353). This exclusive replacement of the Glu 353 of ER by a glutamine fulfils the hydrogen-bonding requirements of the 3-keto steroids. The model proposed for the ligand binding mode of dexamethasone in the human glucocorticoid receptor<sup>9</sup>, in which the D-ring binds between H3 and H6, should therefore be re-examined in the light of our observations.

RAL is a clinically relevant selective antagonist that specifically counters the mitogenic effects of  $E_2$  in the reproductive tissues, while maintaining beneficial oestrogenic effects in other tissues<sup>5,14</sup>.

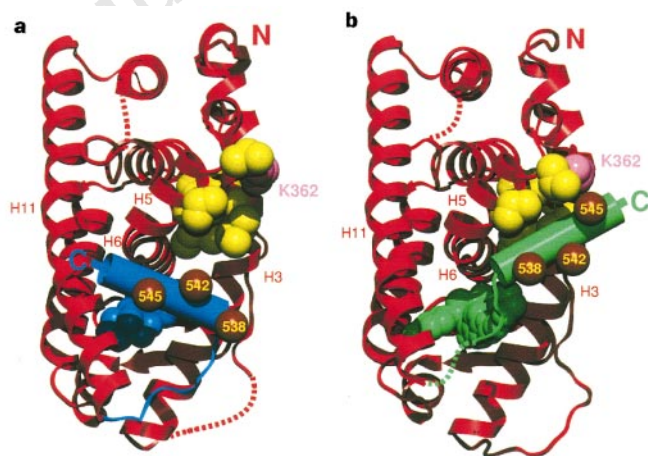


**Figure 3** Positioning of helix H12. Position is shown in **a**, the ER LBD- $E_2$  complex; and **b**, the ER LBD-RAL complex. H12 is drawn as a cylinder and coloured blue ( $E_2$  complex) or green (RAL complex). The remainder of the ER LBD is shown in red. Dotted lines indicate unmodelled regions of the structures. Hydrophobic residues located in the groove between H3 and H5 (yellow) and Lys 362 (K362, pink) are depicted in space-filling form. The locations of Asp 538, Glu 542 and Asp 545 are highlighted (brown spheres) along with the helices that interact with H12 in the two complexes.

RAL binds at the same site as  $E_2$  within the LBD (Fig. 2b,d), with the hydroxyl group of the benzothiophene moiety (O3; see Fig. 2d for atom numbering) mimicking the A-ring phenolic hydroxyl of  $E_2$  by binding in the polar pocket between H3 and H6. In contrast, the binding mode of RAL at the 'D-ring end' of the cavity, between H8 and H11, is markedly different from that of  $E_2$ . Although the phenolic hydroxyl (O11) hydrogen bonds with His 524, it is displaced 5.1 Å from the position occupied by the 17 $\beta$ -OH in the  $E_2$  complex. Consequently, the imidazole ring of His 524 rotates in the RAL complex to compensate for the change in oxygen position and to maintain a favourable hydrogen-bonding position. The remainder of the core is involved in non-polar contacts similar to those seen for  $E_2$ . The side chain of RAL makes extensive hydrophobic contacts with H3 and H5/6, H11 and the loop between H11 and H12. It is anchored to the protein by a direct hydrogen bond between Asp 351 and the piperazine ring nitrogen (N26). However, at over 11 Å in length, the side chain is too long to be contained within the confines of the binding cavity, and instead it displaces H12 and protrudes from the pocket between H3 and H11. This helix displacement is anticipated to be a general feature of both steroidal and non-steroidal anti-oestrogens that possess a bulky side-chain substituent. The importance of the narrow cleft at the A-ring end of the cavity in determining the overall ligand-binding mode is highlighted by the observation that RAL's benzothiophene moiety occupies the same spatial position as the A and B rings of  $E_2$ . The alternate D-ring binding mode of RAL presumably arises as a result of both the inflexibility of the arylbenzothiophene core and the limited scope for positioning the side chain. The orientation of  $E_2$  and RAL should allow the accurate positioning of most of ER's ligands, but further structural studies will be required to understand both the cavity's plasticity and the reported range of different binding modes<sup>15</sup>.

The LBD's transcriptional activation function (AF-2) can interact with a number of putative transcriptional coactivators in a ligand-dependent manner<sup>4,16-18</sup>. Helix 12 is essential for such transactivation as both loss or mutation in this region results in a receptor that is unresponsive to ligand<sup>19</sup>. Mutational analyses in both ER and other nuclear receptors<sup>20,21</sup> have identified several additional residues that influence the function of AF-2, suggesting that the LBD's coactivator recruitment surface, although centred on H12, probably also encompasses parts of the surrounding helices H3, H5/6 and H11.

In the  $E_2$ -liganded complex, H12 sits snugly over the ligand-binding cavity and is packed against H3, H5/6 and H11. Although it makes no direct contact with  $E_2$ , it forms the 'lid' of the binding cavity and projects its inner hydrophobic surface towards the bound hormone. Its charged surface, comprising Asp 538, Asp 545 and the highly conserved Glu 542, is directed away from the body of the LBD on the side of the molecule lying perpendicular to the dimerization interface (Fig. 3a). This precise positioning of H12, which is observed in all known structures of the liganded forms of the LBD<sup>6,7</sup>, seems to be a prerequisite for transcriptional activation as, by sealing the ligand-binding cavity, it generates a competent AF-2 that is capable of interacting with coactivators. In contrast, the alignment of H12 over the cavity is prevented by RAL, and instead the helix lies in a groove formed by H5 and the carboxy-terminal end of H3. This antagonist-induced repositioning of H12 involves a rotation of 130° combined with a 10-Å rigid-body shift towards the amino terminus of the LBD compared with the agonist-induced conformation (Fig. 3b). The complementarity of this hydrophobic groove to the inner surface of H12 suggests that its positioning in the RAL complex represents a real conformation rather than an artefact produced by the crystal lattice. A highly conserved lysine residue (Lys 362), which is required for efficient  $E_2$ -dependent recruitment of certain coactivators<sup>21</sup>, is located at one end of this hydrophobic groove, and is partly buried by the reoriented helix. Taken together, these observations provide compelling evidence

that the antagonistic properties of RAL are based on its ability to prevent the formation of a transcriptionally competent AF-2 conformation. The movement of H12 clearly disrupts the overall surface topography of AF-2, but it is feasible that the tissue selectivity of RAL may reside in its ability to occlude particular coactivator recruitment sites on the surface of the ER LBD.

Selective antagonism of the kind exhibited by RAL is a complicated phenomenon that arises through the interplay of a number of factors, such as differential ligand effects on the transactivation functionalities of the ER, the type of coactivator recruited, and the cell and promoter context<sup>3,4,22,23</sup>. Nevertheless, our data on these structures give valuable insights into the binding of ligands to this receptor, and provide the basis for the structure-based design of improved agonists and antagonists for the treatment of oestrogen-related diseases. □

## Methods

**Protein purification and crystallization.** The LBD of human ER- $\alpha$  (residues Ser 301 to Thr 553) was expressed, purified and carboxymethylated as described<sup>24</sup>. ER LBD-E<sub>2</sub> and LBD-RAL complexes were prepared by including 75  $\mu$ M of the respective ligand in the column elution buffer. The ER LBD is particularly refractive to crystallization, and carboxymethylation of the free thiol groups was essential for growing crystals suitable for diffraction studies. Examination of the electron-density maps shows that Cys 381 is uniformly modified and the remaining three cysteines are either unmodified (Cys 447) or in flexible regions of the structure. The ER LBD-RAL and LBD-E<sub>2</sub> complexes were crystallized using the hanging-drop technique at 18 °C. For the RAL complex, the reservoir solution contained 12% (w/v) PEG 4000, 0.2 M magnesium chloride, 50 mM L-lysine, 0.1 M sucrose and 5% 1,4-dioxane in 0.1 M Tris-HCl, pH 8.5. Hanging drops were composed of equal volumes of protein (7.2 mg ml<sup>-1</sup>) and reservoir solutions. Monoclinic crystals, belonging to the space group C2 with unit cell dimensions  $a = 104.53$  Å,  $b = 53.68$  Å,  $c = 102.71$  Å,  $\beta = 116.79^\circ$  and containing one ER LBD dimer per asymmetric unit, appeared within 2–4 weeks. Two other crystal forms were grown by subtle manipulation of the crystallization conditions (C2,  $a = 89.91$  Å,  $b = 75.09$  Å,  $c = 87.50$  Å,  $\beta = 103.01^\circ$ ; C222<sub>1</sub>,  $a = 65.47$  Å,  $b = 95.99$  Å,  $c = 168.14$  Å). For the E<sub>2</sub> complex, drops containing equal volumes of protein (7–13 mg ml<sup>-1</sup>) and reservoir solution were equilibrated against 0.1 M Tris-HCl, pH 8.1, 2.4 M ammonium formate and 8% dimethylsulphoxide. The E<sub>2</sub> complex crystals belong to the space group P2<sub>1</sub>, with unit cell dimensions  $a = 61.48$  Å,  $b = 115.16$  Å,  $c = 137.38$  Å,  $\beta = 98.8^\circ$ , and contain three ER LBD dimers per asymmetric unit.

**Data collection, phasing and refinement.** For the ER LBD-RAL complex, native diffraction data were collected from a single frozen crystal (120 K) on beamline X11 at EMBL (DESY, Hamburg). Heavy-atom derivatives were collected in-house from flash-frozen crystals. Data were integrated and reduced using the programs DENZO and SCALEPACK<sup>25</sup>. MIR analysis was performed using the CCP4 suite of programs<sup>26</sup>. Diffraction data for the alternate C2 (York) and C222<sub>1</sub> (DESY, Hamburg) crystal forms were collected to resolutions of 3.0 and 3.1 Å, respectively. Initial phases were calculated to 3 Å using MLPHARE<sup>26</sup> and subsequent two-fold averaging, non-crystallographic matrix refinement and phase extension were carried out using DM<sup>26</sup>. An initial polyalanine trace was used to generate a dimeric search model which was correctly positioned in the alternate C2 and C222<sub>1</sub> crystal forms using molecular replacement (AMoRe<sup>26</sup>). Twenty cycles of cross-averaging between all three crystal forms were carried out with DMMULTI<sup>26</sup>, using only the MIR phase information. The resultant electron-density map showed no bias towards the input model and enabled the unambiguous tracing of the remainder of the molecule and the assignment of most of the amino-acid sequence. Refinement was performed with REFMAC<sup>27</sup> using bulk solvent corrections and anisotropic scaling. All data between 25 and 2.6 Å were included with no sigma cut-offs. Tight non-crystallographic restraints were maintained during the initial cycles but were loosened in the final stages of refinement. Phases from multiscrystal averaging were included at all stages and individual atomic temperature factors were refined isotropically. The final model comprises residues 307–459, 470–528 and 535–547. The missing regions correspond to flexible loops between helices H9 and H10 (460–469) and H11 and H12 (529–534) and the chain termini.

Residues Tyr 331(A), Asp 332(A), His 377(B), Glu 397(AB), Lys 416(AB), Glu 419(AB), Glu 423(B), Leu 469(B), Glu 470(AB), Glu 471(AB), Lys 472(AB), Arg 477(AB), Lys 492(A), Glu 542(A), Arg 548(B) and Leu 549(B) were poorly resolved in the electron-density maps and not fully modelled.

For the ER LBD-E<sub>2</sub> complex, diffraction data were collected at room temperature from a single ER LBD-E<sub>2</sub> crystal on beamline X11 at EMBL (DESY, Hamburg). Initial phase estimates were obtained with AMoRe using the refined ER LBD-RAL dimer as a search model. The correct solution, corresponding to three ER LBD dimers, had a correlation coefficient of 69.8 and an *R*-factor of 40.6 after AMoRe rigid-body refinement. Six-fold averaging was performed using DM and the structure was refined with REFMAC using tight non-crystallographic restraints, averaged phases from DM, bulk solvent corrections and anisotropic scaling. All data between 20 and 3.1 Å were included with no sigma cut-offs. A single, overall *B*-value was applied in the early stages of refinement until the *R*<sub>free</sub> converged. Subsequent cycles used tightly constrained, full isotropic *B*-value refinement. The final model for each monomer comprises residues 305–548 but includes two unmodelled loops between residues 331–336 and 462–464. The first four (301–304) and last five (549–553) residues are disordered. The side chains of Leu 306, Leu 466, Leu 469, Lys 492, Lys 531 and Leu 536 were poorly resolved in the electron-density maps and not modelled beyond their C $\beta$  atoms. All model building was carried out using the graphics package QUANTA (Molecular Simulations Inc., San Diego).

**Illustrations.** Figures 1, 2a,b, 3 were prepared with QUANTA (Molecular Simulations Inc., San Diego); Fig. 2c, d was prepared with LIGPLOT<sup>28</sup>.

Received 9 June; accepted 8 September 1997.

- Ciocca, D. R. & Roig, L. M. V. Estrogen-receptors in human nontarget tissues—Biological and clinical implications. *Endocr. Rev.* **16**, 35–62 (1995).
- Tsai, M.-J. & O'Malley, B. W. Molecular mechanisms of action of steroid/thyroid receptor superfamily members. *Annu. Rev. Biochem.* **63**, 451–486 (1994).
- Katzenellenbogen, J. A., O'Malley, B. W. & Katzenellenbogen, B. S. Tripartite steroid hormone receptor pharmacology: Interaction with multiple effector sites as a basis for the cell- and promoter-specific action of these hormones. *Mol. Endocrinol.* **10**, 119–131 (1996).
- Beato, M. & Sánchez-Pacheco, A. Interaction of steroid hormone receptors with the transcription initiation complex. *Endocr. Rev.* **17**, 587–609 (1996).
- Grese, T. A. *et al.* Structure-activity relationships of selective estrogen receptor modulators: Modifications to the 2-arylbenzothiophene core of raloxifene. *J. Med. Chem.* **40**, 146–167 (1997).
- Wagner, R. L. *et al.* A structural role for hormone in the thyroid hormone receptor. *Nature* **378**, 690–697 (1995).
- Renaud, J.-P. *et al.* Crystal structure of the RAR- $\gamma$  ligand-binding domain bound to all-*trans* retinoic acid. *Nature* **378**, 681–689 (1995).
- Bourguet, W., Ruff, M., Chambon, P., Gronemeyer, H. & Moras, D. Crystal structure of the ligand-binding domain of the human nuclear receptor RXR- $\alpha$ . *Nature* **375**, 377–382 (1995).
- Wurtz, J.-M. *et al.* A canonical structure for the ligand-binding domain of nuclear receptors. *Nature Struct. Biol.* **3**, 87–94 (1996).
- Kumar, V. & Chambon, P. The estrogen receptor binds tightly to its responsive element as a ligand-induced homodimer. *Cell* **55**, 145–156 (1988).
- Fawell, S. E., Lees, J. A., White, R. & Parker, M. G. Characterisation and colocalization of steroid binding and dimerization activities in the mouse estrogen receptor. *Cell* **60**, 953–962 (1990).
- Anstead, G. M., Carlson, K. E. & Katzenellenbogen, J. A. The estradiol pharmacophore: Ligand structure-estrogen receptor binding affinity relationships and a model for the receptor binding site. *Steroids* **62**, 268–303 (1997).
- Katzenellenbogen, B. S. *et al.* Antiestrogens: Mechanisms and actions in target cells. *J. Steroid Biochem. Mol. Biol.* **53**, 387–393 (1995).
- Draper, M. W. *et al.* A controlled trial of raloxifene (LY139481) HCl: Impact on bone turnover and serum lipid profile in healthy postmenopausal women. *J. Bone Miner. Res.* **11**, 835–842 (1996).
- Ekena, K., Weis, K. E., Katzenellenbogen, J. A. & Katzenellenbogen, B. S. Different residues of the human estrogen receptor are involved in the recognition of structurally diverse estrogens and antiestrogens. *J. Biol. Chem.* **272**, 5069–5075 (1997).
- Cavallès, V., Dauvois, S., Danielian, P. S. & Parker, M. G. Interaction of proteins with transcriptionally active estrogen receptors. *Proc. Natl Acad. Sci. USA* **91**, 10009–10013 (1994).
- L'Hors, F., Dauvois, S., Heery, D. M., Cavallès, V. & Parker, M. G. RIP-140 interacts with multiple nuclear receptors by means of two distinct sites. *Mol. Cell. Biol.* **16**, 6029–6036 (1996).
- vom Baur, E. *et al.* Differential ligand-dependent interactions between the AF-2 activating domain of nuclear receptors and the putative transcriptional intermediary factors mSUG1 and TIF1. *EMBO J.* **15**, 110–124 (1996).
- Danielian, P. S., White, R., Lees, J. A. & Parker, M. G. Identification of a conserved region required for hormone dependent transcriptional activation by steroid hormone receptors. *EMBO J.* **11**, 1025–1033 (1992).
- Pakdel, F., Reese, J. C. & Katzenellenbogen, B. S. Identification of charged residues in an N-terminal portion of the hormone-binding domain of the human estrogen receptor important in transcriptional activity of the receptor. *Mol. Endocrinol.* **7**, 1408–1417 (1993).
- Henttu, P. M. A., Kalkhoven, E. & Parker, M. G. AF-2 activity and recruitment of steroid receptor coactivator 1 to the estrogen receptor depend on a lysine residue conserved in nuclear receptors. *Mol. Cell. Biol.* **17**, 1832–1839 (1997).
- McInerney, E. M. & Katzenellenbogen, B. S. Different regions in activation function-1 of the human estrogen receptor required for antiestrogen- and estradiol-dependent transcriptional activation. *J. Biol. Chem.* **271**, 24172–24178 (1996).
- McInerney, E. M., Tsai, M.-J., O'Malley, B. W. & Katzenellenbogen, B. S. Analysis of estrogen receptor transcriptional enhancement by a nuclear hormone receptor coactivator. *Proc. Natl Acad. Sci. USA* **93**, 10069–10073 (1996).
- Hegy, G. B. *et al.* Carboxymethylation of the human estrogen receptor ligand-binding domain-

- estradiol complex: HPLC/ESMS peptide mapping shows that cysteine 447 does not react with iodoacetic acid. *Steroids* **61**, 367–373 (1996).
25. Otwinowski, Z. & Minor, W. Processing X-ray diffraction data collected in oscillation mode. *Methods Enzymol.* **276**, 307–326 (1997).
26. Collaborative Computational Project No. 4. The CCP4 suite: programs for protein crystallography. *Acta Crystallogr. D* **50**, 760–763 (1994).
27. Murshudov, G. N., Vagin, A. A. & Dodson, E. J. Refinement of macromolecular structures by the maximum-likelihood method. *Acta Crystallogr. D* **53**, 240–255 (1997).
28. Wallace, A. C., Laskowski, R. A. & Thornton, J. M. LIGPLOT—A program to generate schematic diagrams of protein ligand interactions. *Prot. Eng.* **8**, 127–134 (1995).
29. Laskowski, R. A., MacArthur, M. W., Moss, D. S. & Thornton, J. M. PROCHECK: a programme to check the stereochemical quality of protein structure coordinates. *J. Appl. Crystallogr. A* **42**, 140–149 (1993).

**Acknowledgements.** We thank G. Murshudov for discussions on refinement strategy and J. Baxter, R. Fletcher, S. Nilsson & K. Koehler for comments on the manuscript. The Protein Structure Group at York is supported by the BBSRC. We thank the European Union for support of the work at EMBL DESY/Hamburg through the HEMP access to large installations project.

Correspondence and requests for materials should be addressed to R.E.H. (e-mail: rod@york.york.ac.uk). Coordinates have been deposited at the Brookhaven Protein Data Bank, accession codes 1ERE for the oestradiol-liganded structure and 1ERR for the raloxifene-liganded structure.

## Structure at 1.65 Å of RhoA and its GTPase-activating protein in complex with a transition-state analogue

Katrin Rittinger\*, Philip A. Walker\*, John F. Eccleston, Stephen J. Smerdon & Steven J. Gamblin

National Institute for Medical Research, The Ridgeway, Mill Hill, London NW7 1AA, UK

\* These authors contributed equally to this work.

Small G proteins of the Rho family, which includes Rho, Rac and Cdc42Hs, regulate phosphorylation pathways that control a range of biological functions including cytoskeleton formation and cell proliferation<sup>1–7</sup>. They operate as molecular switches, cycling between the biologically active GTP-bound form and the inactive GDP-bound state. Their rate of hydrolysis of GTP to GDP by virtue of their intrinsic GTPase activity is slow, but can be accelerated by up to 10<sup>5</sup>-fold through interaction with rhoGAP, a GTPase-activating protein that stimulates Rho-family proteins<sup>8,9</sup>. As such, rhoGAP plays a crucial role in regulating Rho-mediated signalling pathways. Here we report the crystal structure of RhoA and rhoGAP complexed with the transition-state analogue GDP.AIF<sub>4</sub><sup>−</sup> at 1.65 Å resolution. There is a rotation of 20 degrees between the Rho and rhoGAP proteins in this complex when compared with the ground-state complex Cdc42Hs.GMPPNP/rhoGAP, in which Cdc42Hs is bound to the non-hydrolysable GTP analogue GMPPNP<sup>10</sup>. Consequently, in the transition state complex but not in the ground state, the rhoGAP domain contributes a residue, Arg 85<sub>GAP</sub> directly into the active site of the G protein. We propose that this residue acts to stabilize the transition state of the GTPase reaction. RhoGAP also appears to function by stabilizing several regions of RhoA that are important in signalling the hydrolysis of GTP.

It has been proposed that GAPs stimulate the intrinsic GTPase activity of the Ras superfamily of proteins either by contributing residues that participate directly in catalysis or by performing an allosteric function (reviewed in ref. 11). We have investigated this question by first determining the structure of p50rhoGAP alone<sup>12</sup> and then as a complex with Cdc42Hs.GMPPNP<sup>10</sup>. From the former structure, we were able to identify residues that could be involved in G-protein binding and GTPase activation. Comparison of this rhoGAP structure with that of p120rasGAP reveals that, although both molecules are predominantly  $\alpha$ -helical, there is no tertiary structural similarity, which is consistent with the lack of any detectable sequence homology between them<sup>10,13</sup>. From the

**Table 1 Data collection and refinement statistics**

Crystal space group: $P2_12_12_1$	
Cell parameters (Å): $a = 66.5, b = 72.0, c = 91.3$	
Data processing	
Observations to 1.65 Å	160,124
Unique reflections	42,992
Completeness (%)	80.5 (60.8)
$I/\sigma$	16.1 (2.3)
$R_{\text{merge}}$ (%) <sup>*</sup>	6.5 (32.4)
Refinement	
Data range (Å)	6.0–1.65
Reflections ( $F > 0$ )	37,875
Non-hydrogen atoms	2,991
Solvent molecules	497
R.m.s. $\Delta$ bond length (Å) <sup>†</sup>	0.013
R.m.s. $\Delta$ bond angles (deg) <sup>†</sup>	1.6
R.m.s. $\Delta B$ -factors for bonded atoms <sup>‡</sup>	2.0
$R_{\text{free}}$ (%) <sup>§</sup>	21.5
$R_{\text{cryst}}$ (%) <sup>§</sup>	16.9

Values in parentheses correspond to the highest-resolution shell (1.76–1.65 Å)

<sup>\*</sup> $R_{\text{merge}} = \sum_i |I_i - \langle I \rangle| / \sum_i I_i$ , where  $I_i$  is the observed intensity and  $\langle I \rangle$  is the average intensity.

<sup>†</sup>Root-mean-squared deviation (R.m.s.  $\Delta$ ) are given from ideal values.

<sup>‡</sup> $R_{\text{free}}$  is the same as  $R_{\text{cryst}}$ , but calculated on the 5% of data excluded from refinement.

<sup>§</sup> $R_{\text{cryst}} = \sum_i |F_o - F_p(\text{calc})| / \sum_i F_p$  for all reflections, where  $F_o$  and  $F_p(\text{calc})$  are the observed and calculated structure amplitudes respectively.

Cdc42Hs.GMPPNP/rhoGAP crystal structure, we were able to show how these two proteins interact in the presence of GMPPNP<sup>10</sup>. Although no interaction between the invariant Arg 85<sub>GAP</sub> and the phosphate moiety of the nucleotide was evident in that complex, we concluded that such an interaction could occur during GTP hydrolysis. We anticipated that Arg 85<sub>GAP</sub> would contribute to catalysis by stabilizing the transfer of charge during transition-state formation, an idea supported by data obtained from the transition-state analogue GDP.AIF<sub>4</sub><sup>−</sup>: binding of p50rhoGAP to RhoA.GDP is enhanced 100-fold in the presence of AIF<sub>4</sub><sup>−</sup>, and this increased binding is abolished if Arg 85<sub>GAP</sub> is mutated<sup>10</sup>. These results suggest that AIF<sub>4</sub><sup>−</sup> acts in the presence of p50rhoGAP and Rho.GDP in a manner similar to that seen in other phospho-transferring enzymes. The crystal structures of several such enzymes, including the G protein G<sub>iα1</sub> (ref. 14), transducin<sup>15</sup> and myosin S1 (ref. 16), have been analysed as complexes with nucleoside diphosphate and AIF<sub>4</sub><sup>−</sup>. These all reveal that the aluminium ion is octahedrally coordinated (with four fluorine atoms defining the equatorial plane), located at a site broadly equivalent to the  $\gamma$ -phosphate position, and coordinated at the apical positions by a  $\beta$ -phosphate oxygen on one side and a water molecule on the other. This arrangement cannot exactly represent the trigonal bipyramidal transition state of a phosphoryl-transfer reaction, although it is probably a good approximation. To examine the proposed role of Arg 85<sub>GAP</sub> in transition-state stabilization, we have crystallized and determined the structure of p50rhoGAP and RhoA.GDP in the presence of AIF<sub>4</sub><sup>−</sup> (Table 1).

The overall structure of the Rho.GDP.AIF<sub>4</sub><sup>−</sup>/rhoGAP complex is shown in a ribbons representation in Fig. 1a. Alignment of the G-protein components of the ground- and transition-state complexes reveals a substantial rearrangement between the G protein and its GAP (Fig. 1b). The two complexes contain different G-protein homologues because we could not crystallize p50rhoGAP with Cdc42Hs.GDP in the presence of AIF<sub>4</sub><sup>−</sup>. However, the residues that contribute to the interface with GAP are strictly conserved between Cdc42Hs and RhoA, suggesting that it is the presence of the transition-state analogue that causes rearrangement of the heterodimer. The movement is essentially a 20° rigid-body rotation of rhoGAP about an axis that runs close to the phenolic hydroxyl of Tyr 66<sub>Rho</sub>. There is a small local change in the structure of the A–A1 loop of GAP which, in combination with the rigid-body rotation, enables the invariant Arg 85<sub>GAP</sub> to interact with the nucleotide. Indeed, the movement of Arg 85<sub>GAP</sub> during the catalytic cycle appears to be the key to the function of p50rhoGAP.

Reproduced with permission of the copyright owner. Further reproduction prohibited without permission.